Research Article Adv. Mater. Lett. 2015, **6**(8), 717-725 Advanced Materials *Letters*

www.amlett.com, www.vbripress.com/aml, DOI: 10.5185/amlett.2015.5874 Published online by the VBRI Press in 2015

Effect of grain size on the structural and magnetic properties of nanocrystalline $Al_3Fe_5O_{12}$ by aqueous coprecipitation method

K. Sadhana[1], S. E. Naina Vinodini[2], R. Sandhya[1], K. Praveena[3,4*]

[1]*Department of Physics, University College of Science, Osmania University, Saifabad, Hyderabad 500 004, India*
[2]*Department of Physics Govt. City College, Nayapul, Hyderabad 500002, India*
[3]*Materials Research Centre, Indian Institute of Science, Bangalore 560012, India*
[4]*School of Physics, Eternal University, Baru Sahib 173101, Himachal Pradesh, India*

[*]Corresponding author. Tel: (+91) 9882699447; E-mail: praveenaou@gmail.com

Received: 26 February 2015, Revised: 13 April 2015 and Accepted: 17 April 2015

ABSTRACT

$Al_3Fe_5O_{12}$ (AIG) nanopowders were synthesized at different pH using aqueous co-precipitation method. The effect of pH on the phase formation of AIG is characterized using XRD, TEM, FTIR and TG/DTA. From the Scherer formula, the particle sizes of the powders were found to be 15, 21, 25 and 30 nm for pH= 9, 10, 11 and 12, respectively. It is found that as the pH of the solution increase the particle size also increases. It is clear from the TG/DTA curves that as the pH is increasing the weight losses were found to be small. The nanopowders were sintered at 900°C/4hrs using conventional sintering method. The phase formation is completed at 800°C/4h which is correlated with TG/DTA. The average grain size of the samples is found to be ~55 nm. As the pH increases the magnetization values are also increasing. The saturation magnetization was found to be 4 emu/g, 6 emu/g, 7 emu/g and 9 emu/g corresponding to pH= 9, 10, 11 and 12, respectively which clearly shows that the magnetization values are dependent on pH. Room temperature magnetization measurements established these compounds to be soft magnetic. The dielectric and magnetic properties (ε′, ε″, μ′ and μ″) of AIG was studied over a wide range of frequency (1GHz-50GHz). With increase of pH both ε′ and μ′ increased. This finding provides a new route for AIG materials that can be used in the gigahertz range. Copyright © 2015 VBRI Press.

Keywords: TG/DTA; magnetic materials; garnets; co-precipitation; dielectric properties; magnetic properties.

Introduction

Since the discovery of iron-containing oxide phases with $A_3B_5O_{12}$ cubic garnet structure have been the subject of extensive investigations because these oxides possess unique magnetic, magneto-optical, thermal, electrical and mechanical properties such as ferrimagnetism, excellent creep and radiation damage resistance, high thermal conductivity, high electrical resistivity, controllable saturation magnetization, moderate thermal expansion coefficients, energy-transfer efficiency, narrow line width in ferromagnetic resonance and others. These properties make iron-containing garnets suitable for numerous device applications, including magnetic materials (circulators, oscillators, phase shifters for microwave region), sensors, lasers, phosphorescent sources, microwave and electrochemical devices [**1**–**4**].

In synthetic garnets with ferromagnetic properties, A is generally a rare-earth cation, and B a transition metal cation. The crystal structure is based on a polyhedral arrangement of oxygen anions defining three kinds of cation sites or sublattices, with dodecahedral (three sites per formula), octahedral (two sites per formula), and tetrahedral (three sites per formula) symmetry, respectively. The dodecahedral sites are normally occupied by the rare-earth cation, while the transition 3d metals enter tetrahedral and octahedral sites. When the transition metal is iron (Fe^{3+}), there is a strong tendency to become ordered in an antiparallel magnetic arrangement. The magnetic moment of a rare-earth cation on dodecahedral sites adds to the octahedral iron's leading to a ferrimagnetic material.

Yttrium iron garnet (YIG) is microwave ferrite in which polycrystalline form has specific characteristics. Substituted yttrium iron garnets have found extensive use in wide band non-reciprocal microwave devices [**5**]. In this family of microwave materials, the polycrystalline aluminium substituted yttrium iron garnets (Y, Al, Fe, and O) have been used in devices where low loss is the major factor. Therefore these systems (Y, Al, Fe, O), have been studied extensively by many investigators [**6-9**]. This is because these materials have a range of magnetization from 300 to 1750 Gauss from $0 \leq x \leq 1.2$ (where non-magnetic $A1^{3+}$ is replacing mostly the tetrahedral Fe^{3+} ions), low resonance line width (ΔH = 40-45 Oe) [**6, 7**] and very low dielectric loss (tan δ, $< 2 \times 10^{-3}$) [**4**] for all the compositions. The aim

of the present work is to develop a low cost materials, to study the effect of Al^{3+} completely replaced at the yttrium site where the properties of $Al_3Fe_5O_{12}$ in meeting the requirements of device engineers. Aluminium based garnets applications are intimately related with its optical properties, chemical stability at high temperatures, good corrosion resistance and mechanical properties.

Recent, survey of literature shows that synthesis of nanocrystalline materials can be done using solid state method [**10, 11**], Co-precipitation [**12**], sol–gel [**13, 14**], microwave hydrothermal [**15**] etc. used for the preparation of nanopowders. The method of preparation strongly determines the structural and magnetic properties of garnets. The main theme of the present work is to develop an electromagnetic absorber which will reduce the electromagnetic pollution which is caused due to the rapid developments of telecommunications and gigahertz electronic systems. It is well known that electromagnetic interference will induce severe interruption of the electronic control system, and it is found that the microwave absorbing material can effectively reduce the electromagnetic backscatter, which is broadly applied in the fields of radar. Currently, various microwave absorbing materials can be obtained, including that to be used in the conditions of high frequency and low frequency [**16**]. Furthermore, the materials with high microwave absorption coefficients, good physical performances and low cost were mainly concerned by the researchers [**17-19**]. This material is going to replace the rare earth based garnets which are very expensive.

Experimental

Materials

A high purity (99.99%, Sigma-Aldrich) chemicals of aluminium nitrate [$Al(NO_3)_3.6H_2O$] and ferric nitrate [$Fe(NO_3)_3.9H_2O$] were used as starting materials, NaOH was used as neutralizer.

Methods

To prepare the aluminum iron garnet by coprecipitation route aluminum nitrate [$Al(NO_3)_3.6H_2O$] and ferric nitrate [$Fe(NO_3)_3.9H_2O$] were taken in 3:5 ratio. The powders were dissolved in hot double de-ionized water and NaOH was added dropwise with controlling of pH ~ 9. The brown precipitation was constantly stirred to obtain homogeneous mixture. The powders were filtered and then washed repeatedly with hot double de-ionized water followed by freeze-drying overnight at 80ºC. The prepared powders were weighted and the percentage yields were calculated from the expected total amount based on the solution concentration and volume and the amount that was actually crystallized. Similar procedure was followed for AIG for pH=10, 11 and 12 by careful, dropwise addition of NaOH.

The phase was confirmed for all the as-prepared powders using Phillips PAN analytical X'pert powder X-ray diffraction (XRD) with Cu-K_α radiation (λ=1.5406Å). Particle size and morphology were determined using transmission electron microscopy (TEM) JEM-2010, JEOL Inc. (Tokyo, Japan). The structural variations of the nanopowders were studied using Fourier transform infrared spectroscopy (FTIR) in the range of 375cm^{-1} to 4000cm^{-1}. Thermogravimetry and differential thermal analysis (TG/DTA) were studied using Rigaku Thermalplus TG 8120 to study the exo–endo temperature of as-received AIG powders. A heating rate of 10°C/min was used in both the TG and DTA measurements upto 1100°C in air. The obtained powders (pH=12) were mixed with an appropriate amount of 2 wt% polyvinyl alcohol as a binder. Then the powder was uniaxially pressed at a pressure of 500 kg/cm^2 to form green pellet specimens. The compacts were sintered at different temperature 800°C/4h using conventional sintering method. The lattice parameters (Å), bulk density (d_b) were determined from the following formulas [**20**],

$$\frac{1}{d_{hkl}^2} = \frac{h^2 + k^2 + l^2}{a^2}$$

Where, d is the interplanar distance and (h,k,l) are miller indices.

$$\rho_{bulk} = \frac{M_{air}}{M_{air} - M_{Xylene}} * \rho_{Xylene} g / cm^3$$

where, M_{air} is mass of the sample in air and M_{Xylene} is mass of the sample in Xylene. The phase and morphology of the sintered samples were studied by using XRD and scanning electron microscopy (SEM). The room temperature saturation magnetization (M_s) and coercive field (H_c) were studied using vibrating sample magnetometer (VSM) Lakeshore 7500, USA upto 15kOe.

The real and imaginary parts of the complex permittivity were measured in the in the microwave frequency range with the help of the Von Hippel method [**21**]. For measurement of the complex dielectric constant, the complex transcendental equation was used. The microwave magnetic field h_{rf} was applied in the plane of the ferrite thin disk (thickness 1 mm, length 0.8mm), which is always normal to an external field.

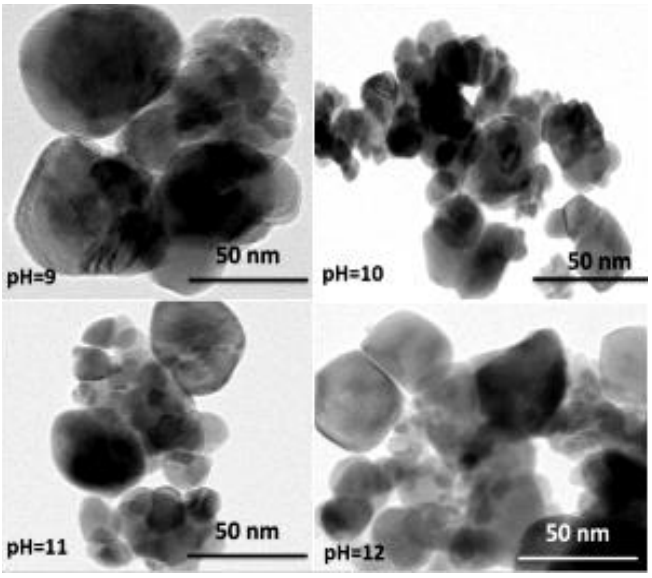

Fig. 1. TEM images of as-synthesized AIG powder of pH=9, 10, 11 and 12.

Results and discussion

Fig. 1 shows the TEM images of as- prepared AIG powder prepared at different pH. TEM images confirm that the particles formed are indeed in the nanoregime. It could be seen from the figure that the powders are spherical in shape and average particle size of the powders are found to be 16 nm, 20 nm and ~ 23 nm for pH 9, 10, 11 and 12 respectively.

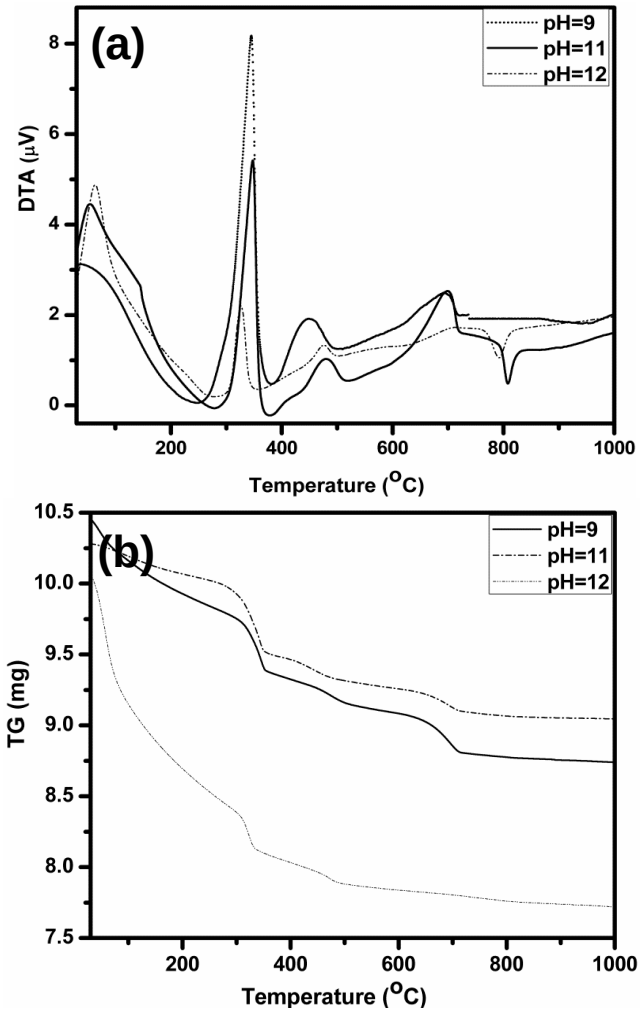

Fig. 2. (a and b). DTA and TG curves of as synthesized powders of pH= 9, 11 and 12.

Fig. 2(a-b) shows the TG/DTA curves for as-synthesized AIG as-prepared powders at different pH. The DTA curve shows four exothermic peaks. The exothermic peak in the range of 60-80°C, 320-340°C, 450-510°C and 680-715°C is due to removal of any absorbed/adsorbed moisture from the sample surface, evaporation of residual nitrate, decomposition of the hydroxides of yttrium and iron into their corresponding metal oxides and the last exothermic peak corresponds to the crystallization of $AlFeO_3$ and AIG, respectively. The results of DTA curves can be correlated to the XRD patterns **(Fig. 4)**. The reaction of formation takes place in the range of 680°C-715°C. The endothermic peak in the range of 740-810°C shows the formation of AIG phase. From the figure it is observed that as the pH is increasing the peaks are becoming narrower and shifting towards the lower temperature region. For pH=12, the pure AIG formation temperature is found to be 790°C, and this has been proved from other researchers [**22, 23**]**.** It could be seen from the Fig.2b that for pH=10 and 11 the variation of weight loss (%) is similar but for pH=12 it is significantly varied. The weight loss corresponds to the temperatures 60- 80°C, 320-340°C, 450-510°C, 680-715°C and 740-810°C for pH=11 were 0.97%, 3.12%, 1.51%, 2.54% and 0.22%, respectively. Similarly for pH=12, 10.79%, 3.34%, 1.25%, 0.25% and 0.20%, respectively. It is concluded that the weight loss (%) decreases with increasing pH. A very small percentage of weight loss is observed in the range of 740-810°C, which shows the formation of AIG phase.

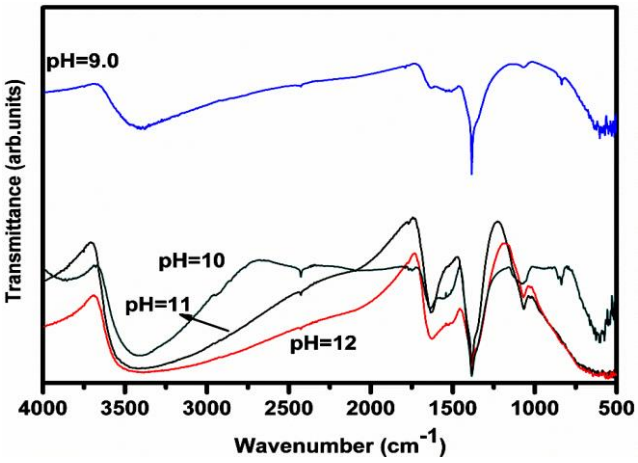

Fig. 3. FTIR spectra of as-synthesized powders of pH=9, 10, 11 and 12.

Fig. 3 shows the FTIR spectra of as synthesized powders of pH= 9, 10, 11 and 12 recorded in the range of 375 cm^{-1} to 4000 cm^{-1}. The bands at 3431 cm^{-1}, 1635 cm^{-1} and 1387 cm^{-1} were assigned to the O-H group, carboxyl group and NO^{-}_{3} ions, respectively. The band at 1400 cm^{-1} was ascribed to splitting anti symmetrical band of carbonate having $C_{2\upsilon}$ symmetry **[24]**. The band at 853 cm^{-1} was corresponds to out of plane bending of CO^{2-}_{3} **[25]**. The three bands at 690 cm^{-1}, 558 cm^{-1} and 455 cm^{-1} were corresponds to the asymmetric stretching (υ_3) of the tetrahedron (Fe–O bond). It could be seen from the figure that the bands become narrower with an increase of pH which suggests that rate of reaction increases between the metal and oxygen atoms.

With increase of pH, the degree of crystallinity also increased progressively. The strong intense vibration bands are observed for the garnet samples that are mostly due to metal-oxygen vibrations. This is treated as highly characteristic for garment structures **[26-28]** depending on the variant valency cationic localities in the garnet crystalline lattice sites.

Fig. 4 shows the XRD patterns of AIG samples sintered at different temperatures. All the XRD peaks were indexed. It could be seen from the figure that at 600°C temperature, it has the phase of $AlFeO_3$ and Fe_2O_3 along with AIG phase is formed. As the sintering temperature increases the reaction between Fe_2O_3 and $AlFeO_3$ increases and which leads to the formation of single phase AIG at 800°C. The formed phases were compared with the JCPDS no: 43-0507 and matches well. No impurity phases were observed. From

the XRD results, the garnet formation can be described as following;

$$Al_2O_3 + Fe_2O_3 \rightarrow 2AlFeO_3 \text{ Occurring at 700°C}$$
$$3AlFeO_3 + Fe_2O_3 \rightarrow Al_3Fe_5O_{12} \text{ Completed at 800°C}$$

The garnet formation temperature could be confirmed from the TG/DTA curves. The lattice constant (Å) is calculated from the value of d_{hkl} corresponding to (1 0 4) as major peak. The values of lattice constant and bulk density were given in **Table 1.** It is found that as the sintering temperature increases, the lattice constant increases, which show the lattice expansion which is likely due repulsive dipolar interactions which are known to influence the crystal structure of nanoferrites **[29]**. As the sintering temperature increases bulk density of the sample increases due to the increase in the particle sizes. The high density was achieved at low sintering temperatures (900°C) due to the smaller particle size of as synthesized powders prepared by this method.

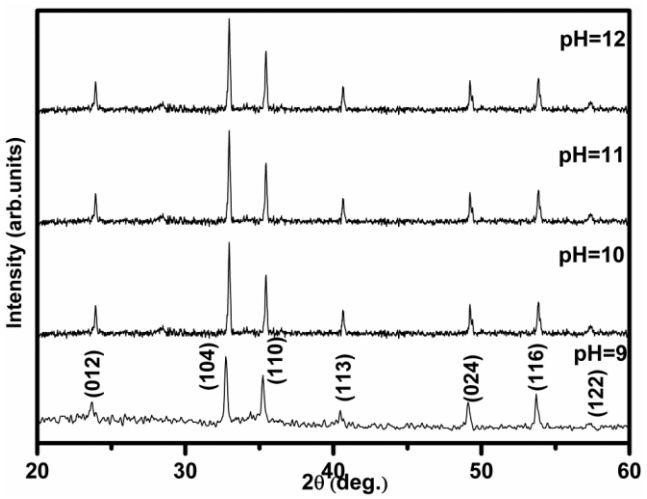

Fig. 4. XRD patterns of AIG powders sintered at 800°C.

Table 1. Grains size, lattice constant, bulk density and Variation of dispersity (measured in the form of Fano factor (σ/d) with respect to sintering temperature. Sintering reduces the polydispersity of YIG particles, synthesized at pH 12.

pH	Lattice constant (Å)±0.001	S_{BET} (m^2/g)	Bulk density (g/cm^3) ±0.04	Grain size (nm)	d (nm)	σ (nm)	(σ^2/d)
9	12.383	104.2	5.13	80	120	28	6.53
10	12.390	106.8	5.22	89	153	32.2	6.77
11	12.396	110.2	5.37	112	174	33.1	6.29
12	12.399	113.3	5.49	125	183	34	6.31

All the diffraction peaks were matched and indexed with the previous report as there are very less reports are available on synthesis of pure $Al_3Fe_5O_{12}$ **[30]**. Using the Scherer's formula, the variations of full-width at half maximum (FWHM) at different XRD peaks indicated that the average crystallite size of the nanoparticles were about 20, 25, 28 and 32 nm corresponding to the pH of 9, 10, 11 and 12, respectively. It is inferred that the size of nanoparticles increased by increasing the pH of the solution. Increase in crystallite size with pH may be associated with the faster particle growth kinetics favored by high pH. The unit cell expansion could be attributed to the increase in the repulsive dipolar interactions at the particle surface due to the existence of unpaired electronic orbital **[31]**. Similar lattice expansion is reported for other nanoparticle oxide system **[29]**.

The specific surface area, (t_{BET}) was calculated by equation:

$$t_{BET} = \frac{F}{S_{BET} D}, \text{ where F is the particle's form factor}$$

(F = 3 for spherical, F = 4 for cylindrical and F = 6 for cubic geometry), S_{BET} is the specific surface area and D is the density. The values of specific surface area for the present ferrites are given in **Table 1** [**32**]. The relatively high SSA associated with Sm^{3+} substituted YIG indicates that it has a lower tendency to agglomerate.

Polydispersity in the sintered samples is measured using an index of dispersion called Fano factor. In this case, it is the ratio of the variance (σ^2) to the mean size (d). Samples with relatively low Fano factor are less polydisperse when compared to those with larger Fano factors. Both the variance and the mean size is obtained using image analysis (performed using ImageJ software) on SEM images. Particles synthesized at pH 12 show the best dispersability. Increase in sintering temperature results in particle size distributions with lower Fano factors, which implies that sintering promotes monodispersity.

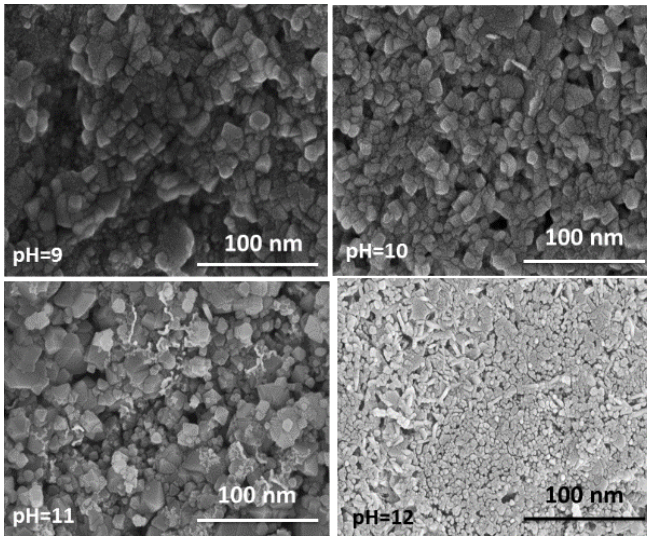

Fig. 5. FE-SEM images of AIG sintered at 800°C.

Fig. 5 show the microstructure of the AIG samples sintered at different temperatures. The morphology of the grains is found to be in spherical shape; over the spherical grains some small sized grains were observed which are attributed to the $AlFeO_3$ phase which can be clearly observed in XRD patterns. The grain sizes at different sintering temperatures are listed in **Table 1**.

The large grain size indicates decrease of grain boundary and surface energy. The average grain sizes of the sintered samples were found to be in the range of 80 nm - 125 nm. The $Al_3Fe_5O_{12}$ sample reveals a cubic structure.

However, when the garnet sample was sintered at high temperature (>800°C) and also of high pH~12, the cubic structure cannot be observed. Both the intrinsic and the extrinsic properties play a role in the observation of the cubic structure. We speculate that intrinsically, it is attributed to the partial occupancy by aluminum ions of the tetrahedron and octahedron [**33-36**], instead of the dodecahedron sites. This is due to the fact that aluminum has a much smaller ionic radius (0.530 Å) compared to that of yttrium (0.892 Å). The larger dodecahedron sites (2.40 Å) are more suitable for the large yttrium ions. All the aluminum ions tend to occupy the octahedron (2.01 Å) and the tetrahedron (1.87 Å) sites, instead of the dodecahedron site as what we expected. Due to the smaller size of aluminium, comparing to the slightly larger ionic radius of the Fe (0.65 Å) and yttrium, there are high tendency of the aluminium to occupy the smaller tetrahedral site. On the other hand extrinsically, the much lower sintering temperature comparing to the conventional ceramic method resulted to the cubic structure.

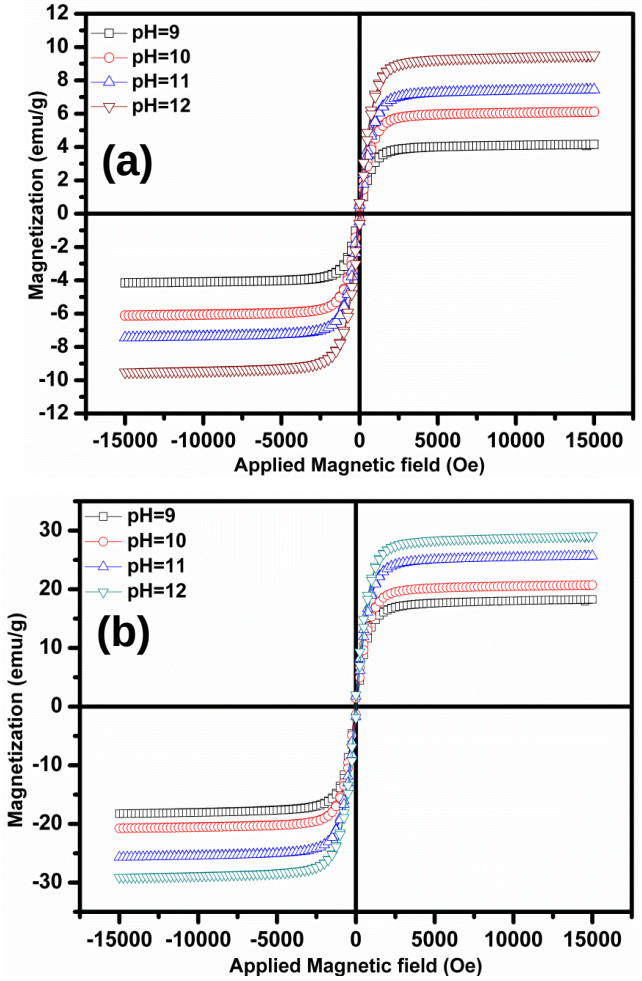

Fig. 6. (a) shows the magnetization curves (M-H) of AIG samples prepared at different pH and (b)shows the magnetization curves of AIG samples sintered 800°C.

Fig. 6(a) shows the magnetization curves (M-H loops) of AIG samples prepared at different pH clearly shows that the samples are magnetic in nature. As the pH increases the magnetization values are also increasing. The saturation magnetization was found to be 4 emu/g, 6 emu/g, 7 emu/g and 9 emu/g corresponding to pH= 9, 10, 11 and 12, respectively which clearly shows that the magnetization values are dependent on pH.

Fig. 6(b) shows the magnetization curves of sintered AIG. Hence the onset of the magnetic moment occurs at a temperature slightly higher than that for the formation of the garnet phase. It is speculated that the difference between the magnetic and crystallographic onset temperatures could be associated with some change in the local ionic coordination around the ferric ions. In general, Fe^{3+} and O^{2-} ions in the garnet form tetrahedrally and octahedrally coordinated ionic clusters. If a deficiency of ions or a local disorder exists in the garnet clusters, the change in the ionic coordination could sensitively alter the super exchange coupling. In the nanoparticle sample, the garnet phase is formed at 600°C but some clusters may still contain some oxygen deficiency. On the other hand, at temperatures higher than 700°C, Fe–O bondings in the clusters could be nearly completed to establish the Fe–O–Fe super exchange couplings which results in the observed onset of magnetization [**37**]. The curves clearly show that all the sintered samples are magnetically ordered. The data of magnetic properties such as saturation magnetization (M_s) and coercive field (H_c) are given in **Table 2**.

It can be seen from the table that as the pH increases the values of M_s increases due to the increase of grain size. The magnetization values depend upon the grain size. According to the relation;

$$M_s(D) = M_s(bulk)\left[1-\frac{\beta}{D}\right]$$

where, M_s (D) is the saturation magnetization of sample with an grain size D, M_s(bulk) is the bulk saturation magnetization value, and β is a constant [**38**]. The experiment result of Fig. 6b is in accord with the formula on the whole. The values of M_s are found to be low as compared with the bulk ferrite [**39**] which is due to the surface anisotropy of the samples [**40**].

The squareness factor (M_r/M_s) also monotonically increases with calcination temperatures, suggesting an increase in magnetocrystalline anisotropy (Table 2). We believe this increase in magnetocrystalline anisotropy is most likely due to improvement in crystal order and structure, expected in samples sintered at high temperatures.

Table 2. Remnant magnetization (M_r), saturation magnetization (M_s) and H_c (coercive field) of AIG sintered at 800 °C.

pH	M_s (emu/gm)	M_r (emu/gm)	M_r/M_s	H_c (Oe)
pH=9	17	2.93	0.17	20
pH=10	19	2.91	0.15	50
pH=11	24	1.48	0.06	90
pH=12	27	1.96	0.072	20

Fig. 7 shows the dependence of coercive field, H_c, on grain size (D). It is observed that H_c increases with an increase of D and further increase of grain size, H_c decreases. The transition from single domain to

multidomain particles will lead to decrease of H_c. The boundary between single domain and multidomain particle is given by critical diameter of the particle (D_c). The critical diameter of the particle is estimated from the formula **[41]**,

$$D_c = \frac{9\sigma_s}{2\pi M_s^2}$$

where

$$\sigma_s = \sqrt{\frac{2k_B T_c[\mathrm{K}]}{a}}$$

where, σ_s is specific wall energy, K is magnetocrystalline anisotropy constant, T_c is Curie temperature, M_s is saturation magnetization, k_B is Boltzmann constant and 'a' is lattice constant. The critical diameter is found to be ~105 nm. The particles sizes below D_c are single domain particles and $D > D_c$ are multi-domain. Therefore, above 800°C the coercivity field decreases with increasing crystallite size due to multi-domain formation and the easy movement of the domain walls.

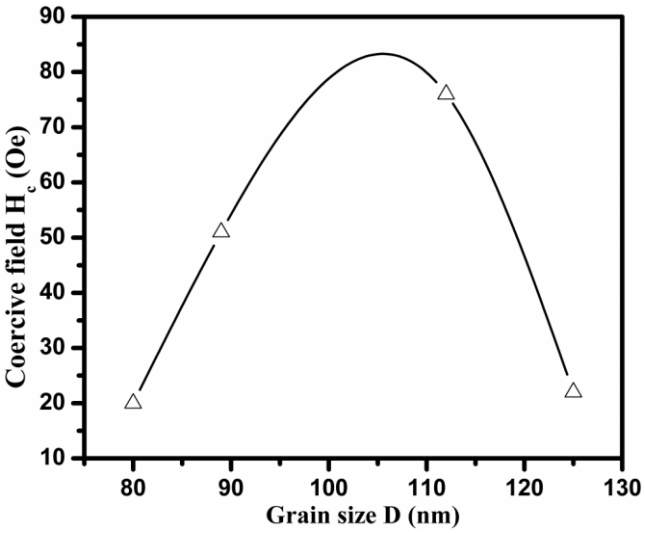

Fig. 7. Coercive field of AIG increases with respect to grain size and sintering temperature. It reaches a maximum at 105 nm; after which H_c decreases. This trend is most likely due to a single domain to multi-domain transition, beyond this grain size.

Fig. 8 (a and **b)** show room temperature the frequency dependent complex permittivity (ε′ & ε″). The complex permittivity and permeability are important for microwave ferrites used at high frequency range. The real part (ε′) is mainly associated with the amount of polarization occurring in the material and the imaginary part (ε″) is related with the dissipation of energy. The complex permittivity and permeability of the samples have been calculated from scattering parameters (S_{11} and S_{21}) using Nicholson- Ross-Weir method [**42, 43**] and shown in Figure. The presence of Al^{3+} results in the formation of more interfaces and a heterogeneous system due to some space charge accumulating at the interface which contributes towards higher microwave absorption in the system. The contribution to the orientational polarization is due to the presence of bound charges (dipoles) [**44**]. Due to the presence of polaron/bipolaron and other bound charges, strong polarization occurs, which leads to high value of ε′ and ε″.

The dielectric constant of any material, in general, is due to dipolar, electronic, ionic and interfacial polarizations. At low frequencies dipolar and interfacial polarizations are known to play the most important role [**45**]. Variations in dielectric constant of ferrites have mainly been attributed to the variations in the concentration of Fe^{2+} ions [**46-48**]. The greater the concentration of these ions, the higher the dielectric constant expected. This is attributable to the comparatively greater polarizability of the Fe^{2+} ions, which have a greater number of electrons than the Fe^{3+} ions. In general, the polarizability of atoms with a larger number of electrons in their outer shells is more than that of atoms having relatively fewer electrons [**49**]. Besides, Fe^{3+} ions have a stable d-shell configuration with spherical symmetry of the charge cloud, on account of their 5d electrons distributed according to Hund's rule. In case of the Fe^{2+} ions, this symmetry is disturbed on addition of an extra electron. Thus, ions would lend themselves to polarization more easily on application of an electric field than the Fe^{3+} ions where the distortion of the spherical charge cloud is relatively more difficult. The presence of Fe^{2+} ions would also result in charge transfer of the type $Fe^{2+} \leftrightarrow Fe^{3+}$, causing a local displacement of electrons in the direction of the electric field leading to polarization. The presence of Fe^{2+} ions, therefore, increases the polarization in ferrites [**50**] and the ferrite containing a larger number of Fe^{2+} ions is likely to exhibit a higher dielectric constant and vice versa.

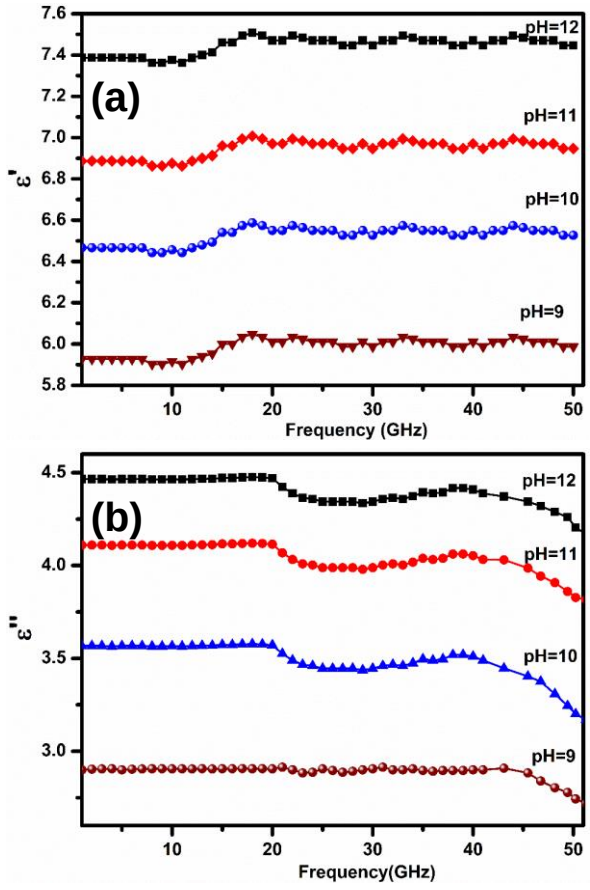

Fig. 8. (a) Frequency variation of real part of permittivity (ε′) and (b) Frequency variation of imaginary part of permittivity (ε″).

It is observed that the dielectric constant (ε′) increases with increasing pH. Dielectric constant in ferrites is contributed by several structural and microstructural factors. The space charge polarization resulting from electron displacement on application of electric field and the subsequent charge build up at the insulating grain boundary is a major contributor to the dielectric constant in ferrites. Therefore, the more the number of Fe^{2+} ions in the ferrite, the more the space charge polarization is expected. It is due to the ease of electron transfer between Fe^{3+} and Fe^{2+} ions and consequently, higher dielectric constant. Now, with sintering temperature, partial reduction of Fe^{3+} to Fe^{2+} takes place. Thus, the value of dielectric constant (ε′) increases with temperature and grain size because of pH.

Fig. 8(b) shows the frequency dependence of dielectric loss AIG sintered at 800°C of different pH. It could be seen from the figure that the value of dielectric loss increases with increase of pH. In general, dielectric loss for polycrystalline ferrites is results due to the lag in polarization vis-a-vis the alternating electric field. This lag increases due to the presence of impurities and imperfections in the garnet structure, "free" charge buildup at interfaces within the bulk of the samples, (interfacial Maxwell-Wagner-Sillars (MWS) polarization **[51]** and the interface between the sample and the electrodes (space charge polarization [**52**]. The polarization in garnets is through a mechanism similar to conduction process thereby increasing the dielectric loss as pH increases. A major contribution to dielectric losses in ferrites comes from electron hopping between the Fe^{2+} and Fe^{3+} ions [**53**].

Fig. 9 (**a** & **b**) demonstrates the variation of real part and imaginary part of magnetic permeability with frequency. Real and imaginary parts of permeability increases with pH. The magnetic loss is caused by the time lag of magnetization vector (M) behind the magnetic field vector [**54**]. The change in magnetization vector is generally brought about by the rotation of magnetization and the domain wall displacement. These motions lag behind the change of the magnetic field and contribute to the magnetic loss (μ″). The rotation of domain of magnetic nanoparticles might become difficult due to the effective anisotropy (magneto-crystalline anisotropy and shape anisotropy) [**55, 56**]. The surface area, number of atoms with dangling bonds and unsaturated coordination on the surface of AIG are all enhanced. These variations lead to the interface polarization and multiple scattering which is useful for the absorption of large number of microwaves.

It is observed that the value of μ' increases with an increase of pH. The real part of the permeability (μ′) represents the real permeability with the magnetization in phase with the alternating magnetic field. The flat μ′ region up to the frequency where it starts declining rapidly gives the compositional stability and quality of prepared ferrite and is known as the zone of utility of the ferrite. And the higher stability of ferrites is a desirable characteristic for various applications such as broadband pulse transformation and wide band read-write heads for video recording etc.,. It is also clear from figure that the permeability is higher as higher the density and grain size, greater the grain to grain continuity in magnetic flux leading to higher permeability [**57**]. That is, when the grain size is smaller, the permeability is lower but the stability is maximum because the presence of small grain size interferes with wall motion.

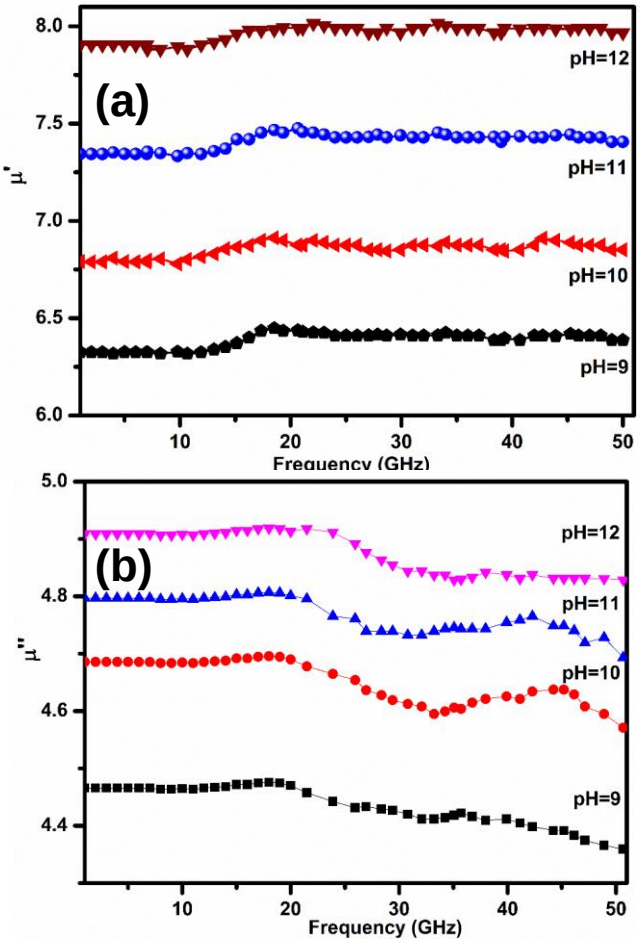

Fig. 9. (a) Frequency variation of real part of permeability (μ′) and (b) frequency variation of imaginary part of permeability (μ″).

Fig. 9(b) show the plots of frequency dependence of imaginary part of permeability (μ"). Again, the losses and their frequency dependence determine the ultimate operating frequency of magnetic devices. The imaginary part of the initial permeability (μ″) represents the loss component when the magnetization is 90° out of phase with the alternating magnetic field. At higher frequencies, losses are found to be lower because the domain wall motion is inhibited and the magnetization is forced to change by rotation. In addition to this, the increase of losses with increase in temperature may be attributed to increase in grain size with sintering temperature and consequently increase in the number and size of magnetic domains which contribute to loss due to delay in domain wall motion.

Conclusion

$Al_3Fe_5O_{12}$ nanoparticles with high H_c, large M_s, easy dispersibility (at pH 12) and easy sinterability (with sintering temperature as low as 800°C) was synthesized by a rapid, low-temperature chemical co-precipitation method. The simplicity and cost-effectiveness of the method ensures easy scaleability. The high yield (96%) of synthesis and the

monodispersity of the resulting particles makes it a viable method for making $Al_3Fe_5O_{12}$ nanoparticles for commercial applications (eg. isolators, magneto- optical devices etc). The average grain sizes, as well as the magnetic properties depend on the sintering temperature. The M_s of 27 emu/g and H_c of 20 Oe were obtained for the samples annealed at 800°C/4h. The critical diameter of the particle is found to be 105 nm. The simplicity of the technique makes it promising for obtaining related ferrite materials, including doped systems. The high values of losses both dielectric and magnetic loss makes these materials promising for defense applications in the GHz (X and K_u bands) range where long range ground surveillance, airborne weather radar, marine radar, police radar etc. and also they can be used to reduce the electromagnetic radiation.

Reference

1. Vaqueiro P.; Lopez-Quintela, M.A.; *Chem. Mater.*, **2011**, *9*, 2836. **DOI:** 10.1021/cm970165f
2. Sadhana, K.; Murthy, S.R.; Praveena, K.; *J Mater Sci: Mater Electron.*, **2014**, *25*, 5130. **DOI:** 10.1007/s10854-014-2282-7
3. Hernandez-Gomez, P.; De Francisco, C.; Torres, C.; Iniguez, J.; Raposo, V.; Perdigao, J.M.; Ferreira, A.R.; *Phys. Stat. Sol. C*, **2004,** *1*, 1792. **DOI:** 10.1002/pssc.200304392
4. Waerenborgh, J.C.; Rojas, D.P.; Shaula, A.L.; Kharton, V.V.; Marques, F.M.B.; *Mater. Lett.*, **2004**, *58*, 3432. **DOI:** 10.1016/j.matlet.2004.05.081
5. Lax, B.; and Button, K.J; Microwave ferrites and ferri-magnetics, McGraw-Hill Book Co. Inc New York, **1962**.
6. Srinivasan, T.T.; Prakash, O.; Patni, M.J.; *Trans. indian. Ceramic Society*, **1981**, *40*, 1. **DOI:** 10.1080/0371750X.1981.10822509T
7. Suresh, K.; Patil, K.C.; J. Alloys Compo. **1994,** *209*, 203. **DOI:** 10.1016/0925-8388(94)91098-7
8. Microwave ferrite materials catalogue, Trans. Tech. Incorporation, Graithsburg, Maryland, USA, **1970**.
9. Multani, M.; Nandikar, N.G.; Venkataramani, N.; Raghupathy, V.; Pansare, A.K.; Gurjar, A.; *Mater. Res. Bull.*, **1979,** *14*, 1251. **DOI:** 10.1016/0025-5408(79)90001-1
10. Renu Rani; Juneja, J. K.; Sangeeta Singh; Raina, K. K.; and Chandra Prakash, *Adv. Mat. Lett.* **2014**, *5(4)*, 229. **DOI:** 10.5185/amlett.2013.fdm.63
11. Radheshyam Rai; Indrani Coondoo; Valente, M. A.; Andrei L. Kholkin, *Adv. Mat. Lett.* **2013**, *4(5)*, 354. **DOI:** 10.5185/amlett.2012.9428
12. *Praveena, K.; Radhika, B.; and Srintah, S.; AIP Conf. Proc.* **2012**, *289*, 1447. **DOI:** 10.1063/1.4709993
13. Usha Chandra; Asokan, K; Ganesan, V.; *Adv. Mat. Lett.* **2013**, *4(11)*, 862. **DOI:** 10.5185/amlett.2013.4455
14. Pittala Suresh; Srinath, S.; *Adv. Mat. Lett.* **2014**, *5(3)*, 127. **DOI:** 10.5185/amlett.2013.fdm.34
15. Sadhana Katlakunta; Sher Singh Meena; Srinath, S.; Bououdina, M.; Sandhya, R.; Praveena, K.; *Mater. Res. Bull.*, **2015**, *63*, 58. **DOI:** 10.1016/j.materresbull.2014.11.043
16. Choopani, S.; Keyhan, N.; Ghasemi, A.; Ali Sharbati, Reza Shams Alam; *Mater. Chem. Phys.*, **2009**, *113*, 717. **DOI:** 10.1016/j.matchemphys.2008.07.130
17. Chawla, S.K.; Mudsainiyan, R.K.; Meena, S.S.; Yusuf, S.M.; *J. Magn. Magn. Mater.*, **2014**, *350*, 23. **DOI:** 10.1016/j.jmmm.2013.09.007
18. Yi Liu; Shicheng Wei; Binshi Xu; Yujiang Wang; Haoliang Tian; Hui Tong; *J. Magn. Magn. Mater.* **2014**, *349*, 57. **DOI:** 10.1016/j.jmmm.2013.08.054
19. Sadhana, K.; Murthy, S.R.; Praveena, K.; *Materials Science in Semiconductor Processing* **2015**, *34* 305. **DOI:** 10.1016/j.mssp.2015.02.056
20. Warren B.E.; X-Ray Diffraction, Addison-Wesley, Reading, MA, **1969**.
21. Von Hippel, A.; Dielectric Materials and Applications, Wiley, New York, **1954**.
22. Praveena, K.; Sadhana, K.; Srinath, S.; Ramana Murthy, S.; *AIP Conf. Proc.*, **2012**, *291*, 1447. **DOI:** 10.1063/1.4709994
23. Praveena, K.; Srinath, S.; *J Magn. Magn. Mater.*, **2014** 349, 45. **DOI:** 10.1016/j.jmmm.2013.08.035
24. Ross, S.D.; Inorganic infrared and Raman spectra, 1st edition, McGraw-Hill, London, **1972**, 150.
25. Rao, C.N.R.; Chemically applications of infrared spectroscopy Academic press, New York, **1963**.
26. Miller, F.A.; Wikins, C.H.; *Anal. Chem.*, **1952,** *24*, 1253. **DOI:** 10.1021/ac60068a007
27. Moenke, H.; Mineral spechtren II Academine, Berlin, **1962**.
28. Wickershein, K.A.; Lefever R.A.; Hanking, B.A.; *J. Chem. Phys.*, **1960**, *32*, 271. **DOI:** 10.1063/1.1700915
29. Ayub, P.; Palkar, V.R.; Chatopadhyay, S.; Multani, M.; *Phys. Rev. B*, **1995**, *51*, 6135. **DOI:** 10.1103/PhysRevB.51.6135
30. Noorhana Yahya, Ramadan Al Habashi Masoud, Hanita Daud, Azizuddin A. Aziz and Hasnah Mohd Zaid, *Am. J. of Engg. & Applied Sci.* **2009**, *2*, 76. **DOI:** 10.3844/ajeassp.2009.76.79
31. Ayub, P.; Multani, M.; Barma, M.; Palkar, V.R.; Vijayaraghavan, R.; *J. Phys. C.*, **1988**, *21*, 2229. **DOI:** 10.1088/0022-3719/21/11/014
32. Lowell, S; Shields, J.E.; Thomas, M.A.; Thommes, M.; Characterization of Porous Solids and Powders: Surface Area, Pore Size and Density, (Kluwer Academic Publishers, ordrecht/Boston/London, **2004**.
33. Vaqueiro, P.; Crosnier-Lopez, M.P.; Lopez-Quintela, M.A.; *J. Solid State Chem.*, **1996**, *126*, 161. **DOI:** 10.1006/jssc.1996.0324
34. Potdevin, A.; Chadeyron, G.; Boyer, D.; Mahiou, R.; *J. Non-Cryst. Solids*, **2006** *352*, 2510. **DOI:** 10.1016/j.jnoncrysol.2006.03.046
35. Mc Currie, R.A.; Ferromagnetic Materials: Structure and Properties, Academic Pr. University of Michigan, **1954**, 352.
36. Chen, Y.F.; Wu, K.T.; Yao, Y.D.; Peng, C.H.; You, K.L.; Tse, W.S.; *Microelect. Eng.*, **2005**, *81*, 329. **DOI:** 10.1016/j.mee.2005.03.028
37. Kim, T.; Nasu, S.; Shima, M.; *J. Nanopart. Res.*, **2007** 9, 737. **DOI:** 10.1007/s11051-006-9082-9
38. Sanchez, R.D.; Rivas, J.; Vaqueiro, P.; Lopez- Quintela, M.A.; Caeirob, D.; *J. Magn. Magn. Mater.*, **2002**, *247*, 92. **DOI:** 10.1016/S0304-8853(02)00170-1
39. Guo, X.Z.; Ravi, B.G.; Devi, P.S.; Hanson, J.C.; Margolies, J.; Gambino, R.J.; Parise, J.B.; Sampath, S.; *J. Magn. Magn. Mater.*, **2005**, *295*, 145. **DOI:** 10.1016/j.jmmm.2005.01.007
40. Metselaar, R.; Huyberts, M.A.H.; *J. Phys. Chem. Solids*, **1973**, *34*, 2257. **DOI:** 10.1016/S0022-3697(73)80074-5
41. Smit, J.; Wijn, H.P.J.; Les Ferrites, Dunod, Paris, **1961.**
42. Nicolson, A.M.; Ross, G.F.; *IEEE Trans. Instrum. Measur.*, **1970** 19, 377. **DOI:** 10.1109/TIM.1970.4313932
43. Weir, W.B.; Proc. IEEE, **1974**, *62*, 33. **DOI:** 10.1109/PROC.1974.9382
44. Phang, S.W.; Hino, T.; Abdullah, M.H.; Karamoto, N.; *Mater. Chem. Phys.*, **2007**, *104*, 327. **DOI:** 10.1016/j.matchemphys.2007.03.031
45. Hedvig, P.; Dielectric Spectroscopy, edited by I.R. Macdonald (Wiley, New York) **1987**.
46. Kyritsis, A.; Pissis P.; Grammatikakis, J.; J. Polym. Sci. Polym. Phys., **1995**, *33*, 1737. **DOI:** 10.1002/polb.1995.090331205
47. Singh, A.K.; Goel, T. C.; Mendiratta, R.G.; *J. Appl. Phys.*, **2002**, *91*, 6626. **DOI:** 10.1063/1.1504493
48. Rezlescu N.; Rezlescu, E.; *Phys. Stat. Sol. a*, **1974**, *23*, 575. **DOI:** 10.1002/pssa.2210230229
49. Irvine, J.T.S.; Huanosta, A.; Velenzuela, R.; West, A.R.; *J. American Ceram. Soc.*, **1990**, *73*, 729. **DOI:** 10.1111/j.1151-2916.1990.tb06580.x
50. Koops, C.G.; *Phys. Rev*, **1951**, *83*, 121.

DOI: 10.1103/PhysRev.83.121
51. Hench, L.L; West, J. K.; Principles of Electronic Ceramics, John Wiley and sons, New York, **1990**, 346.
52. Brockman F.G.; White, R. P.; *J. American Ceram. Soc.*, **1971**, *54*, 183.
DOI: 10.1111/j.1151-2916.1971.tb12259.x
53. Van Uitert, L.G.; *Proc. IRE.*, **1956**, *44*, 1294.
DOI: 10.1109/JRPROC.1956.274952
54. Ishino, K.; Narumiya, Y.; *American Ceramic Society Bulletin*, **1987**, *66*, 1469
ISSN: 0002-7812
55. Dimitrov, D.A.; Wysin, G.M.; *Phys. Rev. B*, **1995,** *51*, 11947.
DOI: 10.1103/PhysRevB.51.11947
56. Shilov, V.P. ; Bacri, J.C.; Gazeau, F.; Gendron, F. ; Perzynski, R.; Raikher, Y.L.; *J. Appl. Phys.*, **1999**, *85*, 6642.
DOI: 10.1063/1.370173
57. Verma, A.; Chatterjee, R.; *J. Magn. Magn. Mater.* **2006**, *306*, 313.
DOI: 10.1016/j.jmmm.2006.03.033